UNIVERSITY *of* VIRGINIA

Methods for Analyzing Microglial Signaling and Cortical Spreading Depression Wavefronts in 2-Photon Calcium Images

A thesis presented to
the faculty of
School of Engineering and Applied Science
University of Virginia

In Partial Fulfillment
of the Requirements for the Degree
Master of Science in Electrical Engineering

By

MARK FILIP SLUZEWSKI

JULY 2019

VIRGINIA IMAGE & VIDEO ANALYSIS

Advisor: Prof. Scott T. Acton

Abstract

Cortical spreading depressions are a neurological phenomenon that occur most notably during strokes and traumatic brain injury, characterized by slowly propagating waves of near-complete neuron depolarization followed by prolonged suppression of neuron activity. While their cause and purpose is still poorly understood, it is believed that they play a role in activating microglia, leading to the release of pro-inflammatory cytokines into the brain. Microglial activation is also believed to promote the occurrence of further cortical spreading depressions. The added neurological stress and inflammation induced by cortical spreading depressions can exacerbate injury to the brain. As a result, suppressing their generation and downstream effects has become a topic of interest in medical research, with microglia as a potential target. In this effort, 2-photon fluorescence microscopy and calcium imaging has been used in recent years to generate image sequences of cortical spreading depression propagation and subsequent microglial activation through calcium-based signaling. Due to the novelty of such images, methods for consistently analyzing such image sequences have not been presented within the literature. This thesis contributes to solving this issue in two distinct ways. The first is by presenting a workflow for segmenting microglia and measuring their calcium-based signaling in response to cortical spreading depressions. The second is a novel image segmentation algorithm for segmenting the wavefront boundary of cortical spreading depressions.

ACKNOWLEDGEMENTS

This thesis could not have been done without the help of many people. First, I would like to thank my advisor, Dr. Scott Acton, for the tremendous support, wisdom and mentorship. I would also like to thank Dr. Petr Tvrdik and his team for allowing me to collaborate with the Center for Brain Immunology and Glia, and for providing access to resources and performing the imaging necessary to complete this project. I would also like to extend gratitude to Dr. Daniel Weller for his advice and guidance, as well as serving as the chair of the committee.

I would also like to thank the members of Virginia Image and Video Analysis lab for the abundance of support and guidance. In particular, great thanks to Tiffany Ly for her advice in writing this thesis, as well as her dog, Maddy, for the emotional support her presence provided.

I would like to thank my parents, Renata Dolecka and Jarek Sluzewski for the support and motivation these last 24 years. Finally, I would like to thank my dear friends Tyler Ealy, Micheal Sheridan, and Matthew Heavner for their continuous friendship and support throughout my studies at the University of Virginia.

AUTHOR'S DECLARATION

I declare that the work in this thesis was carried out in accordance with the requirements of University's Regulations and Code of Practice for Research Degree Programs. Except where indicated by specific reference in the text, the work is the candidate's own work. Work done in collaboration with, or with the assistance of, others, is indicated as such. Any views expressed in the dissertation are those of the author.

SIGNED: ..... DATE: .....

TABLE OF CONTENTS

List of Tables

Table **Page**

List of Figures

Figure **Page**

CHAPTER 1

INTRODUCTION

Permanent damage to the central nervous system (CNS) due to stroke and traumatic injury is one of the leading causes of morbidity in the US. However, despite decades of medical and scientific research into this topic, there is still much that is poorly understood about the neurological and immunological phenomena associated with such injuries and their causes. Furthermore, there are relatively few methods of treatment to reduce the cascade of pathological phenomena that occur and increase damage to the CNS, worsening patient outcome and survivability.

One phenomena that is particularly poorly understood is referred to as a cortical spreading depression (CSD) or spreading depolarization. A CSD is characterized by a wave of near-complete neuron and astrocyte depolarization, followed by suppressed neural activity, which propagates through the CNS, starting from tissue surrounding the point of injury. While single occurrences of CSDs are associated with migraine auras with no permanent damage, they occur repeatedly and with increasing intensity following a stroke or traumatic injury [4, 5]. The prolonged metabolic stress of repeated, large-scale depolarizations can damage otherwise healthy neurons and even result in

apoptosis. The immune response that occurs alongside CSDs, primarily tissue inflammation, leads to further stress on the tissue and reduced oxygen supply. This combination of phenomena exacerbates the injury, leading to further cell death and reduced patient outcome [1, 6, 7].

Despite the existence of CSDs being known for over 70 years, and having been clinically observed in humans for 18 years, very little is known about their cause and the mechanisms behind their effects, and there is no clinicaly approved method for inhibiting them or reducing their detrimental effects [8]. A primary reason for this is that CSDs have mostly been observed with electrodes and laser speckle contrast imaging (LSCI), which do not provide information about the underlying cellular mechanics that cause and drive them. However, innovations in transgenic mouse models and fluorescent microscopy in recent years have begun to allow us to image CSDs and their effects *in vivo* at the cellular level [1]. However, due to the novelty of these imaging techniques, few methods for processing and analyzing such images have been presented, and no standard approaches have been codified.

1.1 Overall Methodology and Challenges

The goal of this thesis is to contribute to the developing field of CSD imaging by presenting methods which can be used to analyze *in vivo* image sequences of microglia responding to CSDs which are aquired through confocal fluorescent microscopy. The contributions of this thesis are divided between two projects. The first contribution is presenting a workflow for analyzing the microglia's signalling response to the cortical spreading depression in fluorescent microscopy image sequences. This workflow is a combination of traditional image and video preprocessing techniques and a novel method for removing background signals from the fluorescent trace of a microglia based on the Gram-Schmidt Process. The second contribution is a novel image segmentation method designed to segment the wavefront boundary of a CSD as it propagates through the image. This is a local region-based

segmentation method which overcomes many of the extreme occurrences of noise and intensity inhomogeneity present in such images.

Despite the successes of the methods presented in this thesis, there are still some challenges which can be improved upon in future work. The signal denoising process presented in the analysis workflow is sensitive to the timing between when the signal of the CSD appears in the local region versus the region of interest of a microglia. Though this lag is very small in the image sequences used in this thesis, future iterations may benefit from additional methods which correct for this. Furthermore, the effectiveness of the image segmentation method presented is dependent on a proper initialization of the algorithm, as the active contours generated are rigid and do not allow for significant adjustments to the overall shape to correct for errors during the optimization process.

1.2 Thesis summary

The objective of this thesis is to develop new methods of analyzing *in vivo* fluorescent microscopy images of CSDs and their effects on microglial signalling. Chapter 2 provides an overview of the background of CSDs, their potential link to microglia, and the challenges of segmenting CSDs. Chapter 3 proposes a workflow for preprocessing, segmenting and analyzing the fluorescent response of microglia as they respond to CSDs through calcium signalling. Chapter 4 describes a novel segmentation algorithm for segmentation of CSD wavefronts which overcomes many of the challenges which hinder traditional methods. Chapter 5 summarizes the findings from Chapters 3 and 4 and provides suggestions for future work.

CHAPTER 2

BACKGROUND OF CORTICAL SPREADING DEPRESSIONS AND CONFOCAL SEGMENTATION

2.1 Cortical Spreading Depressions

CSDs are a pathological neurological phenomena associated with traumatic brain injury, stroke, and migraines. They are characterized by a slowly-propagating (1.7-9.2mm/min) wave of near-complete neuron depolarization, followed by a period of suppressed neural activity. In traumatic brain injuries and stroke, CSDs occur repeatedly with increasing intensity over time, causing metabolic stress that damages healthy neurons and exacerbates the injury [4, 5]. Because of this, research into the causes of CSDs, the neurological and immunological responses they induce, and methods of inhibiting their generation and effects are important to improving patient outcome.

While CSDs and their role in brain injury have been investigated in previous studies, these primarily relied on the use of electrodes for *in vivo* recording of their generation and propagation[4]. In recent years, researchers have begun to use two-photon microscopy to image CSDs on a cellular scale as the

propagate through the brain [1]. These imaging studies are particularly useful in investigating the suspected role of non-neuronal cells, such as microglia, in the generation of CSDs and the resulting cellular response [1, 6, 7]. In these studies, the propagation of the CSD is detected through calcium indicators (such as GCaMP) which fluoresce in response to increased intracellular calcium [9]. In this paradigm, the CSD appears as a region of increased fluorescence as neuronal dendrites depolarize in the focal plane, which rapidly propagates through the image as a wavefront.

2.1.1 Relationship Between Microglia and Cortical Spreading Depressions

Microglia are the primary immune cell within the central nervous system (CNS). They bear functional similarity to macrophages that reside in the rest of the body, but are characterized by long processes which survey surrounding neurons when in resting state. Microglia are responsible for both fine-tuning synaptic function and responding to infections and injury. This gives them a significant role in the progression of strokes and traumatic brain injury. The removal of microglia from the brain leads to an increase in tissue damage and a deregulation of neuronal activity following an ischemic stroke [7]. At the same time, the removal of microglia inhibits the generation of CSDs following such injury [8], suggesting an important role in their generation. A potential mechanism for this is the release of tumor necrosis factor-alpha (TNFα) during microglial activation in response to stroke or brain injury, which increases neuron excitability [8, 10]. The release of pro-inflammatory cytokines may further enhance this behavior [8, 11]. While microglial activation appears necessary for the generation of CSDs, evidence in the literature also indicates that CSDs play a role in activating microglia during stroke and traumatic injury [8]. This potentially suggests a positive feedback relationship between the two phenomena, whereby the injury causes initial CSDs and local microglial activation, leading to the release of TNFα, inducing further CSDs which in

turn stimulate more microglia to release TNFα. This potential relationship provides a possible target for intervention and treatment. If microglial activation and release of TNFα and pro-inflammatory cytokines is inhibited, CSDs generation may be suppressed, reducing injury and improving patient outcome.

Unfortunately, little is known about microglial cellular biology and mechanisms of activation, due to the difficulty of loading fluorescent dyes, the lack of effective receptor and channel inhibitors, and their sensitivity to activation in both *in vivo* and *in vitro* environments [8, 12]. However, it is believed that changes in intracellular pH and ion concentrations though intercellular signalling, release of internal ion reservoirs, and influx through membrane-bound ion channels play important roles in many forms of microglial activation [12]. An ion of particular interest is calcium (Ca^{2+}). Increases in intracellular calcium, due to both release of internal stores and influx from the intercellular environment, is a common component in cellular responses to external stimuli for most cell-types within the CNS [13]. Furthermore, suppression of microglial calcium signalling through drug-based inhibition of calcium-release activated calcium (CRAC) channels has been demonstrated to decrease microglia pro-inflammatory activity during traumatic brain injury [6]. This means that measuring changes in intracellular calcium levels is an effective method for quantifying microglial activation in response to CSDs. Furthermore, it may serve as a promising target for drugs designers to inhibit this activation.

2.2 *In Vivo* Fluorescent Microscopy Imaging and Segmentation

In vivo imaging of the central nervous system has become an increasingly prevalent approach to neuroscience research. Advances in transgenic animal models and two-photon microscopy have allowed researchers to directly ob-

serve the development and behavior of many cells and structures within the brain which hitherto have only been approximated through *in vitro* studies and indirect observation [1, 14, 15]. Such imaging is often performed by introducing a fluorescent protein, through endogenous genetic engineering or viral-based delivery, into the desired tissue or cells. The fluorescent proteins allow for the direct imaging of cells and their underlying structures and protein [1, 16]. However, due to the complexities of the tissues being imaged, this technique has several challenges which affect image and segmentation quality. The primary challenge is that tissue is adept at scattering light, which results in noise and decreasing fluorescent intensity as the imaging depth increases [16]. This problem of noise and clarity is compounded by the fluorescence of tissue outside the focal plane, as well as partial or total occlusion of objects in the image by more opaque structures that lie above the focal plane, such as blood vessels[16]. Because of these difficulties, the development of robust image segmentation strategies, both for general and specific applications, is critical to successful analysis.

2.2.1 Challenges in Segmenting Cortical Spreading Depression Wavefronts

Accurately segmenting the boundary of the CSD can provide valuable information about which regions have undergone depolarization in a given image, as well as measuring the direction and speed of the CSD. However, as a result of light scattering and occlusion, *in vivo* images of CSDs are often characterized by a low signal-to-noise ratio (SNR), intensity inhomogeneity, and discontinuities in the CSD's wavefront. These obstacles make delineating the wavefront difficult for many segmentation methods which rely on edge detection or global information. Traditional approaches to segmentation of biological images such as active contours [17, 18], level set methods [19], and watershed techniques [20] fail due to poor contrast and inhomogeneity of the observed intensity. This is because the low SNR can make it challenging to

accurately calculate edges within the image, while the intensity inhomogeneity and discontinuities make it challenging to calculate a global statistic that properly distinguishes the depolarized regions from the rest of the image. This results in segmentations where the contour boundary fails to advance towards the CSD wavefront or ones which "sink into" the discontinuous or inhomogeneous regions of the wavefront, resulting in poor segmentations.

CHAPTER 3

MEASURING MICROGLIAL CALCIUM SIGNALLING DURING CORTICAL SPREADING DEPRESSIONS

In this section, a workflow for segmenting microglia and measuring their calcium signalling in response to CSDs is presented. As part of this workflow, a novel method for removing the background fluorescence caused by the CSD from the microglia's fluorescent trace is presented. This workflow is used to examine the efficacy of inhibiting microglial activation through the use of the CRAC channel-inhibiting drug CM-EX-137, which is a potential method for reducing brain inflammation during strokes and traumatic injury.

3.1 *In Vivo* 2-Photon Imaging of Cortical Spreading Depressions

In order to directly image the propagation of CSDs *in vivo* at a cellular level, the use of 2-photon fluorescent microscopy and calcium imaging is required. This allows for the direct imaging of cells that are otherwise opaque and

obscured by the surrounding tissue, as well as visualizing of cellular processes occurring within them. In this project, images of CSDs were acquired using mice that were a genetic cross between the Cre-dependent genetically encoded calcium reporter [21] and the Iba1(Aif1)-IRES-Cre lines [13]. This leads to the expression of two fluorescent proteins within the mouse CNS. The first protein is tdTomato, with microglia being the primary cell that expresses it. This acts a marker, labeling the microglia in the image with a red color that allows for easier visualization and segmentation. The second protein is GCaMP5G, a Ca^{2+} indicator. This means that an increase in Ca^{2+} in a cell's microenvironment through depolarization or the release of internal stores leads to an increase in fluorescence by GCaMP5G [1].

In order to image CSD within the mouse CNS, a cranial window was mounted on the top of the skull. CSDs were induced through either a middle cerebral artery occlusion (MCAo) to induce an ischemic stroke or by injection of 1M of potassium chloride (KCl) into the brain. Imaging was performed using a 2-photon microscope with red and green emission filters at a focal depth of between 100-200 μm with a resolution of ~0.9 μm per pixel. 512 x 512 image sequences were recorded over 20 minutes with an imaging frequency of 2.5 Hz,

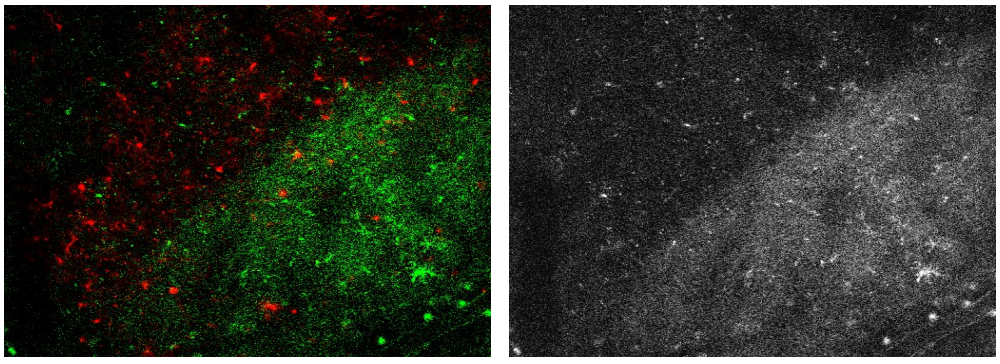

Figure 3.1: (*left*) Multi-photon microscopy image of a cortical spreading depression (CSD). Microglia (red) respond to calcium signalling from the rapid depolarization of neurons (green) [1]. (*right*) Isolated green-channel image of CSD. Brighter regions indicate areas which have already undergone depolarization.

for a total of 3075 images per sequence. To reduce data size during analysis, these sequences were trimmed to 400 frames (~160s) with approximately 200 frames before and after the CSD appears in the image. See Figure 3.1 for an example of an image acquired with this method.

The generation of transgenic mice, surgery, and imaging was performed by Dr. Petr Tvrdik and his students in the Center for Brain Immunology and Glia at the University of Virginia.

3.2 Image Sequence Stabilization with SURF Features

Muscle spasms are a common symptom of strokes, including mice, which can cause challenges when analyzing *in vivo* microscopy image sequences during such conditions. This comes in the form of motion artifacts and shifts in the focal plane which can cause static structures in the image to change location over the course of the imaging session, complicating the task of calculating time-dependent features, such as changes in fluorescent intensity, using fixed regions of interest (ROI). Generating these ROI by segmenting a mean intensity projection (MIP) of the sequence is also challenging, as the motion blurs the boundaries of structure in the MIP. While it is possible to use an adaptive ROI which moves along with the cell in the image, the small size of the microglia and high SNR in images at this resolution leads to a lack of detail and increased difficulty in accurately segmenting individual frames of sequence. One method to overcome this is to preprocess the sequence with a motion correction algorithm which stabilizes the image and maintains a fixed location for the cells over the course of the image sequence. The motion correction method utilized in this project has three major steps. First, a feature extraction algorithm is applied to the current frame in the sequence to serve as potential points of reference. Second, the features are matched to similar features in the initial frame of the sequence in order to estimate the

motion between frames. Third, a geometric transformation is applied to the current frame that minimizes the distance between these matched features and corrects for the motion.

3.2.1 SURF Feature Extraction

The feature extraction process used in this project utilizes the speeded up robust features (SURF) method [22]. The SURF method detects blob structures within an image, which makes it well suited for detecting the blob-like structure of microglia cell bodies, or soma. SURF uses a determinant-of-Hessian (DoH) approach to determine strong features within the image. The Hessian matrix, $H(x,\sigma)$, of a pixel within an image, x, at a scale, σ, is defined as:

$$H(x,\sigma) = \begin{bmatrix} L_{xx}(x,\sigma) & L_{xy}(x,\sigma) \\ L_{yx}(x,\sigma) & L_{yy}(x,\sigma) \end{bmatrix} \tag{3.1}$$

where $L(x,\sigma)$ is the convolution between the image and a kernel of the Gaussian second-order derivative, $\frac{\delta^2}{\delta x^2} g(\sigma)$. For a given pixel, the determinant of its Hessian matrix is used as a metric to determine the strength of a candidate feature, with pixels above a given threshold being labeled as features [22]. To reduce the number of redundant features, only the pixel with the largest determinant in a local region is labeled as a feature. In order to improve the robustness of detected features, as well as constrain the range of sizes of blob-like features detected, the image is evaluated with multiple kernels of varying size and scale [22]. The different sets of such kernels are often referred to octaves, with a higher octave corresponding to larger filter sizes. Here, 3 filters from the second octave were used, corresponding to filters of size 15x15, 27x27, and 39x39 pixels.

Once a the feature is located within an image, it is given a set of descriptors that uniquely describes the characteristics of the local region surrounding that feature's location. In the SURF algorithm, two values are used as the descriptor. The first is the dominant orientation of the region [22]. This is

calculated through the Haar-wavelet responses in the x and y directions within $6s$ pixels of the point, where s is the scale of the kernel size used when the feature was detected, relative to the smallest kernel size for the octave. This is done on a subsampled version of the region, where the step size between samples is also s. The scale of the wavelets used are also s. The second is a description of the local region within a $20s$ window centered on the point of interest [22]. This region is subdivided into 4x4 subregions, where the Haar-wavelet responses in the x and y directions of each subregion is summed and weighed by a Gaussian function ($\sigma = 3.3s$). The orientations of the x and y axis for this calculation are with respect to the dominant orientation of the region, i.e. the x axis is parallel to the dominant orientation and the y axis is orthogonal to that orientation.

In this project, feature extraction is performed on the red channel of each frame, where the microglia are labeled with tdTomato. In order to reduce the amount of noise in each frame, and strengthen potential features, a median filter is applied to the image prior to feature extraction. Due to the high SNR of the images despite this filtering, a low determinant threshold of 50 was used to maximize the number of potential features. Naturally, this can result in a very high number of poor features. This is constrained by only considering the 50 features with the strongest determinants in future steps of the motion correction algorithm.

3.2.2 Feature Matching

Once features have been extracted from the current frame in the image sequence, it is possible to determine which correspond to features detected in the initial frames of the sequence. The method used in this project is an exhaustive comparison between the local region descriptors of each feature using the sum of square differences (SSD) as a metric (Figure 3.2). By this method, the difference between the local region descriptors of a feature in the

initial frame, f', and a feature in the current frame, f, is given by

$$SDD(f, f') = \sum_{i=1}^{n} (f_{ix} - f'_{ix})^2 + (f_{iy} - f'_{iy})^2 \tag{3.2}$$

where f_i and f'_i are the i^{th} local region descriptors of each feature, out of the n total for each feature. Because these descriptors of the local region are computed in relation to the dominant orientation of the feature, this comparison is robust against rotation [22]. The two features which have the lowest SDD score between them are designated as matching features.

Due to relative simplicity of the images being compared, it is possible for two features that do not correspond to the same object to be matched under with this method (see Fig. 3.2). Attempting to minimize the distance between such erroneously matched features when calculating the motion-correcting transformation, especially when there are few matching features, can result in significant errors in the final result. In order to account for such errors, the euclidean distance between each pair of matched features is calculated. If this distance exceeds 20 pixels, or approximately 18 μm, the pair is removed from

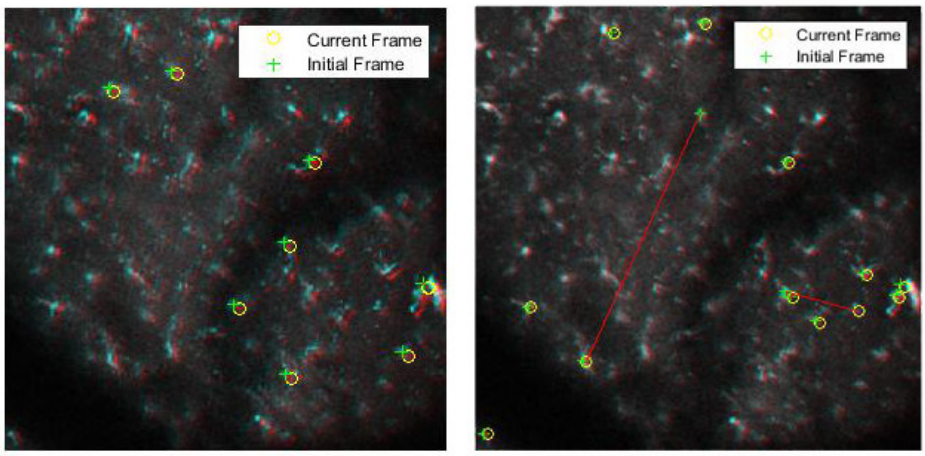

Figure 3.2: Examples of matched features between image sequence frames. (*left*) Matching features between two frames in a image sequence. (*right*) Example of two features being incorrectly matched due to the simplicity of the images (*red*).

consideration. This threshold was derived empirically from an observation of the image sequences used in this thesis and can be tuned if necessary in future applications of this method. The use of the initial frame of the sequence as a reference, as opposed to the previous frame post-correction, is to reduce the effects of accumulating error as the algorithm processes each frame of the image.

3.2.3 Estimating Geometric Transformation with MLESAC

Once matching features have been identified, one can deform the image through geometric transformations, such as translation and rotation, so that the features in the current frame align spatially with their matches in the initial frame. This corrects for the motion that has occurred in the time between these two frames, leading to an image sequence where fixed objects remain in the same spatial location throughout the sequence. One method that can be used to perform is called an affine transform matrix [23, 24]. Multiplying this matrix, $\boldsymbol{T}$ with the spacial coordinates of a pixel, $\boldsymbol{x} = [x, y, 1]$, yields the new coordinates for that pixel in the transformed image, $\hat{\boldsymbol{x}} = [u, v, 1]$ like so:

$$\boldsymbol{x}\boldsymbol{T} = \hat{\boldsymbol{x}} \tag{3.3}$$

$$[x, y, 1] \begin{bmatrix} a & b & 0 \\ c & d & 0 \\ e & f & 1 \end{bmatrix} = [u, v, 1] \tag{3.4}$$

The transformation performed by the affine transformation matrix allows for three types of geometric transformations: rotation, translation, and skewing [23, 24]. This accounts for both the displacement and rotation that occurs in the image sequences during motion artifacts, as well as the the subtle skewing of the image that might occur due to shifts in the orientation of the focal plane. As the new image generated is larger in size than the original image, due to

some pixels moving to locations outside the original boundaries, the result is cropped back to the original size with respect to how it aligns with the reference image.

In this project, the Maximum Likelihood Estimation Sample Consensus (MLESAC) method is used to estimate the affine transformation matrix [25]. This is done by minimizing a cost function that calculates the maximum likelihood estimation (MLE) error between the coordinates of the target feature, $\boldsymbol{x}' = [x', y', 1]$ and the new coordinates of its matched feature according to the current iteration of the transformation matrix, $\hat{\boldsymbol{x}} = [u, v, 1]$. The MLE error of the i^{th} feature pair is calculated as

$$e_i = (u_i - x_i')^2 + (v_i - y_i')^2 \tag{3.5}$$

The cost function is

$$c = \sum_i p(e_i^2) \tag{3.6}$$

$p(e^2)$ is an error term given by

$$p(e^2) = \begin{cases} e^2 & e^2 < T^2 \\ T^2 & e^2 \geq T^2 \end{cases} \tag{3.7}$$

where $T = 1.96\sigma$, σ being the standard deviation of the MLE errors in the current iteration [25].

3.3 Microglia Segmentation

With potential motion artifacts corrected in the image sequence, it is now possible to specify regions of interest (ROI) in the image which can be used to measure changes in fluorescence which correspond to microglial calcium signalling. A simple way of generating these ROI is to segment the microglia in the MIP of the sequence through some segmentation algorithm, such as active contours. Active contours are an attractive solution because they allow for the segmentation of complicated shapes by iteratively evolving a contour towards

features that indicate the boundaries of the object being segmented [3, 26–30]. This often leads to a high degree of accuracy in the final segmentation, and many active contour methods have been developed for biologically-related tasks such as fluorescent microscopy images [2, 3, 31, 32]. In this project, the Tubularity Flow Field (TuFF) algorithm is used to perform this segmentation [32].

3.3.1 The TuFF Algorithm

TuFF is an example of a level set-based active contour designed for segmenting tubular structures such as neurons, blood vessels, and microglia [32]. In level set methods, the image is represented as a higher-dimensional, continuous function, ϕ, called the level set function [33, 34]. Within ϕ, every pixel, x, is given some scalar value, $\phi(x)$. Generally, positive values are given to pixels belonging to the object being segmented, and negative values for pixels in the background, with the zero-level, $\phi(x) = 0$, defining the boundaries of the contour. The level set is first initialized by the user or some automated method in order to provide a rough estimation of the object being segmented. An energy functional, $\varepsilon(\phi)$, is used to iteratively modify ϕ through gradient descent by using local or global information to evolve the contour boundaries to the edges of the object [33, 34]. In the TuFF algorithm, this energy functional is defined as

$$\varepsilon(\phi) = \varepsilon_{reg}(\phi) + \varepsilon_{evolve}(\phi) + \varepsilon_{attr}(\phi) \tag{3.8}$$

$$\varepsilon_{reg}(\phi) = v_1 \int_{\Omega} |\nabla\phi(\boldsymbol{x})|\delta(\phi)d\boldsymbol{x} \tag{3.9}$$

$$\varepsilon_{evolve}(\phi) = -\int_{\Omega} \sum_{i=1}^{d} \alpha_i \langle \boldsymbol{v_i}(\boldsymbol{x}), \boldsymbol{n}(\boldsymbol{x})\rangle^2 H(\phi)d\boldsymbol{x} \tag{3.10}$$

In this equation, $\varepsilon_{reg}(\phi)$ serves to moderate the curvature of the active contour, with higher values of the regularization parameter, v_1, leading to smoother

contours. $\varepsilon_{evolve}(\phi)$ is the primary portion of the energy functional driving curve evolution, with an emphasis on evolving the contour towards the boundaries of tubular structures [32]. $\delta(\phi)$ and $H(\phi)$ are the dirac and heaviside functions respectively. $\boldsymbol{n(x)} = \frac{\nabla\phi(x)}{|\nabla\phi(x)|}$ is the inside normal vector of the level set and $\boldsymbol{v_i(x)}$ is the i^{th} eigenvector of the Hessian of the image at a given pixel, which combine to drive the boundaries of active contour towards the edges of tubular structures [32]. $\varepsilon_{attr}(\phi)$ is an additional functional which helps to compensate for discontinuities and intensity inhomogeneity in the image by driving together boundaries that are close to each other[32].

It should be noted that there is a variation of the TuFF algorithm, TuFF-BFF, which is more specialized for microglia segmentation [35]. However, the small size of most microglial soma in the image sequences as well as the lack of detail in microglia processes, both due to a high SNR, lead to the conclusion that the advantages of this method were not significant enough to have an appreciable effect on segmentation results.

3.3.2 ROI Generation with TuFF

In order to segment the microglia in each image sequence, the MIP of the red channel is first generated. This is a pixel-wise time-averaging of pixel intensities that removes noise and creates a more well-defined structure for each microglia, which improves segmentation results. The original implementation of TuFF utilized the Otsu threshold as a method of automatically initializing the level set [32, 36]. However, the small size of microglia and the high SNR present the MIP images results in large portions of background being contained within the initialized contour, which significantly reduces the accuracy of segmentations and introduces the need for several additional post-processing steps to refine results and remove erroneous segmentations. Therefore, a manual initialization scheme was used. Each microglia in the MIP was identified and initialized with one or more elliptic initial contours. The TuFF algorithm was then run for 300 iterations. Fine-tuning of hyperparameters was necessary in some cases to improve results. The resulting level

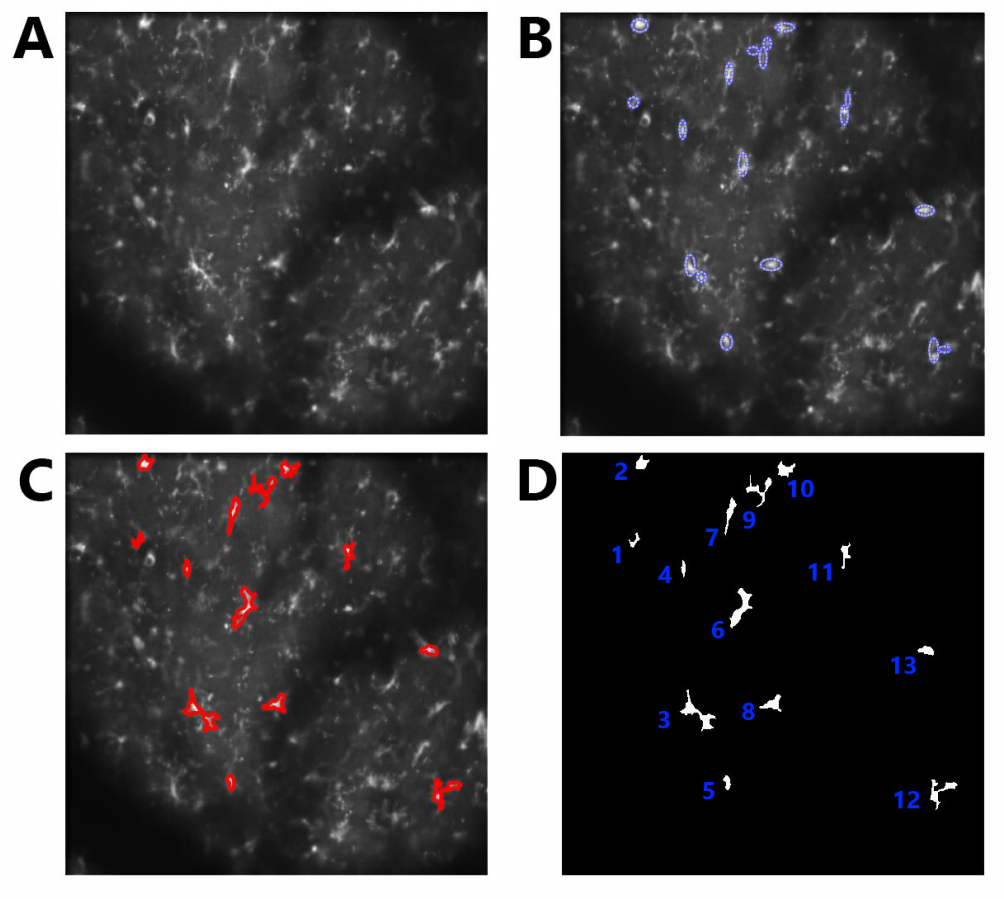

Figure 3.3: Intermediate steps of ROI generation with TUFF: (*a*) MIP of the red channel of the image sequence after motion correction. (*b*) Initialization of level set. Pixels within the initial contours (*blue*) will have values of 1 and pixels outside will have values of -1. (*c*) Final segmentation contours (*red*) of TUFF algorithm. (*d*) Final level set is thresholded and individual binary objects are labeled as individual microglia.

set is thresholded at the zero-level to produce a binary representation. Each binary object in the segmentation was given a numerical label and designated as a separate ROI. See Figure 3.3 for an example of this process.

3.4 Calculating Microglia Fluorescent Trace

In order to measure the activation of microglia through calcium signalling, it is necessary to quantify changes in the fluorescence of GCaMP5G within the microglia after stimulation by the CSD. One popular and effective way of doing this is by computing the fluorescent trace of the ROI [37–39]. This is a normalized measurement of the mean pixel intensity within the ROI over time, calculated with the following equation:

$$Trace(t) = \frac{\Delta F(t)}{F_0} = \frac{F(t) - F_0}{F_0} \tag{3.11}$$

where $F(t)$ is the mean pixel intensity at time t and F_0 is a baseline intensity, often calculated as the average mean intensity of the ROI during a resting state prior to whatever response that is being measured [37–39]. In order to measure the intracellular calcium signalling of the microglia in response to CSDs, the fluorescent trace of the green channel for each segmented ROI is independently measured. The baseline fluorescence is calculated as the average fluorescence in the initial 100 frames (~40s) of the image sequence. In order to improve the SNR of the signal, each trace is filtered using a wavelet filter followed by a 1D median filter [40].

3.4.1 The Local Region-Corrected Fluorescent Trace

Two common features used for quantifying the results of fluorescent trace calculations are the peak intensity and area-under-curve (AUC) of the fluorescent response being measured [37–39]. These values measure the strength of the response being measured and its duration, respectively. However, in the context of measuring microglial calcium signalling in response to CSDs, calculating these values can be complicated by background signals. This is because GCaMP5G is expressed both in microglia and a subset of neurons in the mouse lines used. While this allows for the visualization of the CSD as it propagates through the image, it introduces background signals into the ROI, in the form of neural dendrites above the microglia in the focal plane depolarizing. When

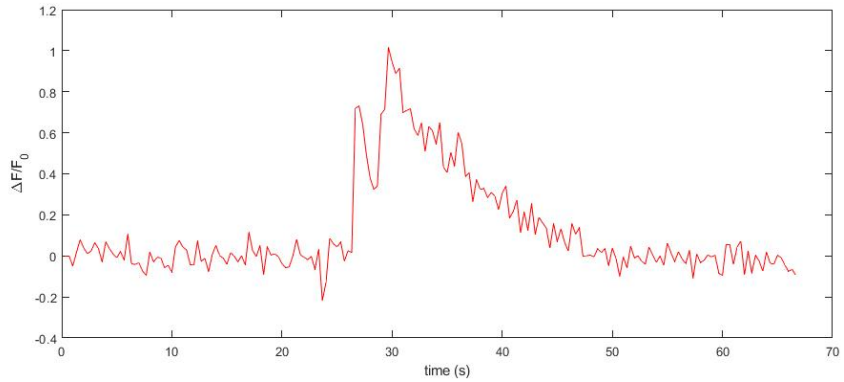

Figure 3.4: Microglial trace prior to denoising. The first peak in the trace is a background signal from the CSD while the second is from the microglia's fluorescence.

using a ROI of the microglia, this background signal introduces a second fluorescent response into the resulting trace (Figure 3.4). This background signal often overlaps with a portion of the microglia's calcium signalling in response to the CSD, which often lags behind the CSD by ~1-3s. Calculating the peak intensity and AUC of such a trace produces erroneous results, as the background signal can increase both values. Additionally, in cases where microglia do not respond significantly to the CSD, this background signal is even more prominent within the trace, leading to values which erroneously indicate a response. Therefore, it is necessary to removes this background signal.

In order to remove the background signal from microglial fluorescent traces, this project presents a novel modification of the traditional approach, called the Local Region-Corrected Trace (LRCT) (Figure 3.5). In this approach, an additional trace of the microglia's local region is calculated, which records the background signal independently of the microglia. The local region is defined as pixels that have a euclidean distance of 5-10 pixels, 4.5-9 um, from the boundary of the microglia's ROI. The local region trace is then used to remove the background signal from the microglial trace through the use of the Gram-Schmidt Process [41]. The result is a version of the microglia's trace

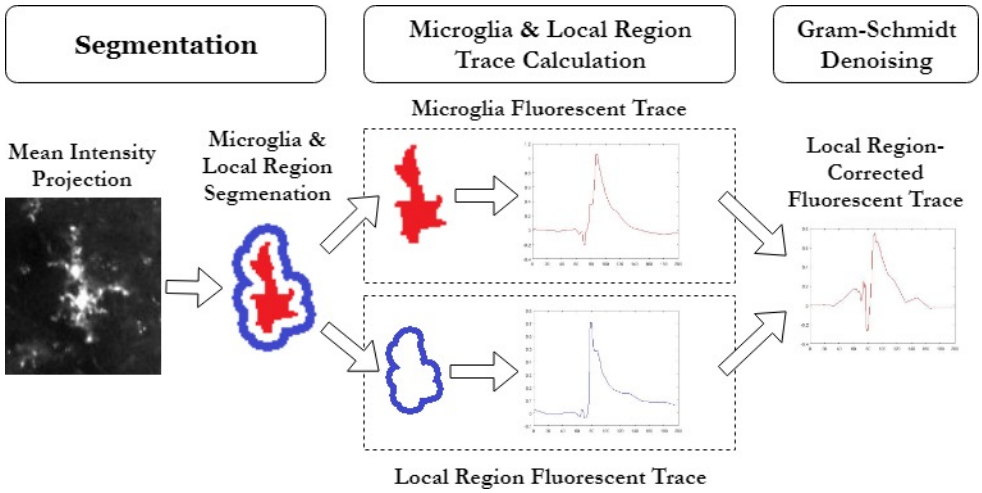

Figure 3.5: Diagram of Local Region-Corrected Trace method.

which has had this background signal removed.

3.4.2 Gram-Schmidt Process

The Gram-Schmidt Process is a method of orthonormalization, similar to Principle Component Analysis [41]. It is used in linear algebra to decompose linearly independent vectors into orthogonal basis vectors, but it has also seen application in denoising applications for approximating an underlying signal from a noisy representation. This is because a noisy 1D signal can be modeled as the linear combination of two vectors, one for the signal and the other for the noise [42, 43]. The basic principle of the Gram-Schmidt Process is based on calculating the projection of a reference vector onto a vector you wish to decompose. By subtracting this projection from the vector, you obtain a vector that is orthogonal to the reference vector. The equation for obtaining this orthogonal vector is

$$\boldsymbol{u_2} = \boldsymbol{v_2} - proj_{\boldsymbol{u_1}}(\boldsymbol{v_2}) \tag{3.12}$$

$$proj_{\boldsymbol{u_1}}(\boldsymbol{v_2}) = \frac{\langle \boldsymbol{v_2}, \boldsymbol{u_1} \rangle}{\langle \boldsymbol{u_1}, \boldsymbol{u_1} \rangle} \boldsymbol{u_1} \tag{3.13}$$

where $\boldsymbol{v_2}$ is the vector being decomposed and $\boldsymbol{u_1}$ is the reference vector [41]. In the context of signal denoising, $\boldsymbol{v_2}$ is the noisy signal and $\boldsymbol{u_1}$ is an estimation of the noise in the signal over time. The result is a denoised signal [42].

3.4.3 Removing Background Fluorescence with Gram-Schmidt Process

As stated in the previous section, the Gram Schmidt Process can be used to denoise a signal using an estimation of the noise contained in the signal. In this case, we will use the Gram-Schmidt Process to remove the background signal from the microglia's trace, using the local region trace as an estimation of the signal.

In order to improve the accuracy of the denoising process, both signals are first split into two separate, overlapping sections of uniform length. Each segment has a 50% overlap with the other. This introduces a level of redundancy in the signal removal process, with the most significant portions of the signal being denoised twice. Each of these sections is shifted to have a mean of 0 and normalized prior to the use of Gram-Schmidt:

$$\hat{\boldsymbol{s_i}} = \frac{\boldsymbol{s_i} - a_i}{m_i} \tag{3.14}$$

$$a_i = mean(\boldsymbol{s_i}) \tag{3.15}$$

$$m_i = max\{\boldsymbol{s_i} - a_i\} \tag{3.16}$$

where $\boldsymbol{s_i}$ is a section of a trace. This improves the effectiveness of the signal removal by reducing the magnitude of the scalar values being calculated [41]. Once each section has been preprocessed in this manner, they are collected into two matrices, $\boldsymbol{M}$ and $\boldsymbol{L}$, for the microglia and local region traces, respectively. Each row of a matrix is a separate section of the split signal. Once this is done, the Gram-Schmidt Process is performed as a matrix operation,

$$\boldsymbol{D} = \boldsymbol{M} - \frac{\boldsymbol{M} \cdot \boldsymbol{L}}{\boldsymbol{L} \cdot \boldsymbol{L}} \boldsymbol{L} \tag{3.17}$$

where $\boldsymbol{D}$ is the partitioned signal with the background signal removed, and $\cdot$ is the dot product. The division and multiplication in this equation are performed elementwise. The shifting and normalization is then reversed using the same scalar values used previously on the microglia trace:

$$\boldsymbol{s_i} = a_i \hat{\boldsymbol{s_i}} + m_i \tag{3.18}$$

Once the sections have been restored to their original scale, they are recombined into a single signal, with overlapping portions being averaged together. The result is a fluorescent trace of the microglia which has had the background fluorescence from the CSD removed (Figure 3.6).

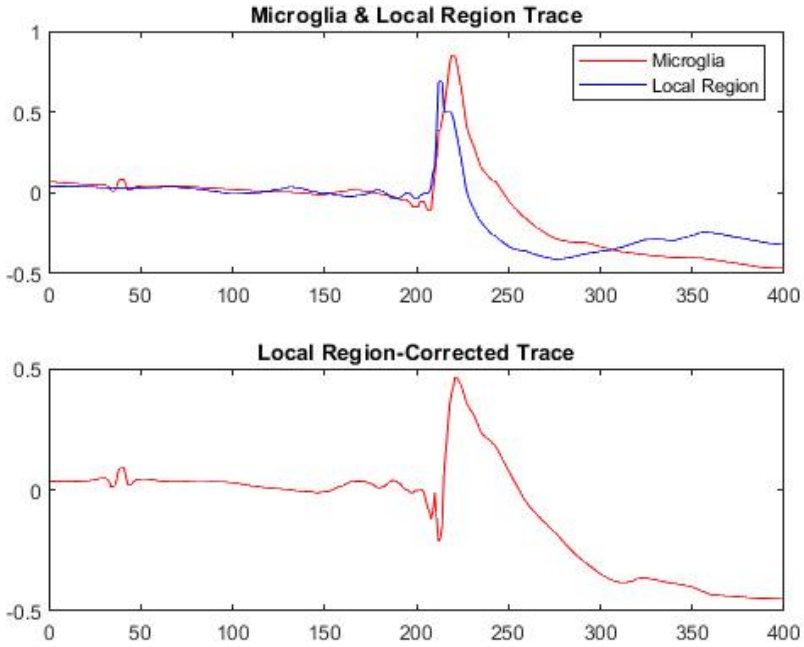

Figure 3.6: (*top*) Microglial and local region traces. (*bottom*) Microglial local region-corrected trace.

3.5 Validation Experiment: Effects of CRAC Channel Inhibition on Microglial Calcium Signalling

In order to provide an example of the workflow presented in this project, in particular the LRCT, we will use it to quantify the effects of CM-EX-137 on microglial calcium signalling during CSDs. CM-EX-137 is a novel CRAC channel inhibitor which reduces the buildup of intracellular calcium in microglia [6]. The influx of intracellular calcium though the CRAC channel is believed to be an important step in the signalling cascade of a microglia's activation and pro-inflammatory response during strokes and traumatic injury[8]. In support of this theory, CM-EX-137 has been shown to suppressing the activation and pro-inflammatory response of microglia during experimental brain trauma, reducing lesion size and neuronal death as well as improved neurological outcome [6]. This potentially makes it the first drug treatment which can be used to reduce the detrimental effects of CSDs. In the original study, quantification of the effects of CM-EX-137 was performed through histological and immunofluorescent analysis of brain slices post-treatment, as opposed to direct *in vivo* imaging [6]. If similar results can be inferred by applying the workflow proposed in this project to *in vivo* image sequences of CSDs, it would serve as validation of the approach.

Six mice of the same line described in Section 2.1 were used, with one mouse was treated with CM-EX-137 and another treated with the drug vehicle as a control. CSDs were induced through the injection of KCl into the brain approximately 60s into the imaging session. Three image sequences were taken from each mouse. These were then preprocessed and analyzed using the described process and peak fluorescence was calculated from the background-corrected traces. As a demonstration of the effectiveness and necessity of the LRCT, peak fluorescence values were also calculated for traces of the CM-EX-137 positive sequences prior to applying the LRCT approach.

As predicted, the use of CM-EX-137 lead to a noticeable reduction in the occurrence and strength of microglial calcium signalling as a result of CSD (Figure 3.7). Qualitatively, the was a significant reduction in the number of microglia which fluoresced in response to the CSD when treated with CM-EX-137, and those that did had a noticibly reduced intensity. The mean peak intensity for microglia in the control case was 0.450±0.0.167 while the mean for mice treated with CM-EX-137 was 0.171±0.145, a statistically significant difference. Importantly, the mean peak intensity for microglia in the CM-EX-137 group prior to applying the LRCT method was 0.312±0.161, which is a less in line with predictions from the literature. Conclusions on the effectiveness of CM-EX-137 based on such results could have been misleading. This result confirms the necessity of removing background signals when analyzing microglial

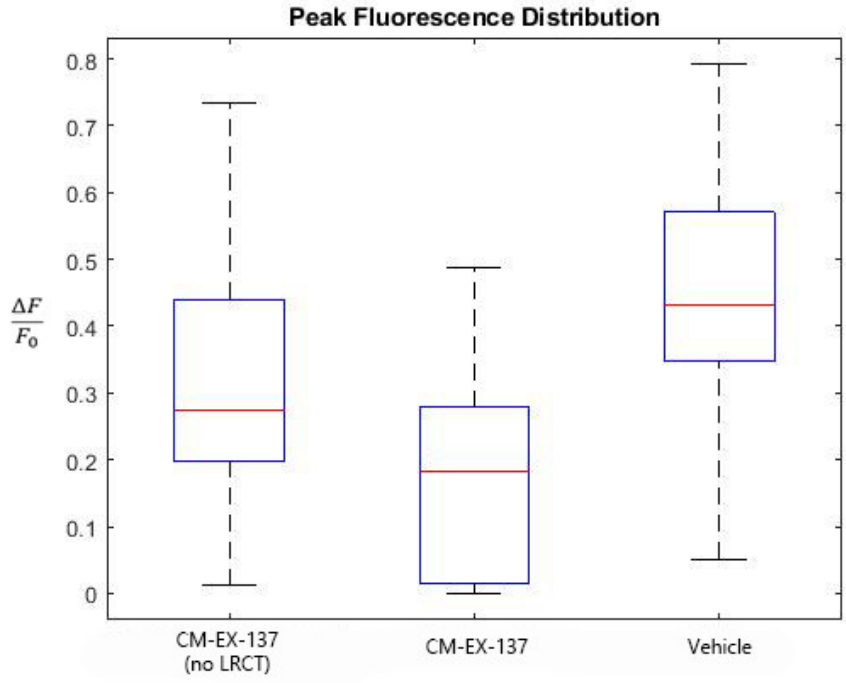

Figure 3.7: Distributions of peak intensity values for microglia treated with CM-EX-137 and the vehicle (control). Results for the CM-EX-137 treated mice prior to the application of the LRCT method are included for comparison.

fluorescence, and supports the efficacy of the LRCT method in accomplishing this.

3.6 Discussion

In this chapter, we presented a workflow that can assist researchers in analyzing microglial activation in response to CSDs. The efficacy of this method has been validated through use on a real-world experiment, bearing the results in agreement with the literature. By adopting this general methodology, we hope that future researchers will have an easier, standardized method of conducting research on this topic and improve our understanding and treatments of stroke and traumatic brain injury. Despite the successes of this workflow, there is still room for improvement that can be iterated on in future work. The primary downside of using the Gram-Schmidt Process, as described in Section 3.4.3, is that it operates on each element of the signal relatively independently. That is, it assumes that both the noisy signal and noise model are in near-perfect alignment with respect to time. This makes the method sensitive to delays between the onset of fluorescence from the CSD in the local region trace compared to the microglia trace. If this delay is significant enough, the background fluorescence will not be completely removed in the resulting trace. In the imaging sequences used in this project, this delay was not present or trivial, as 2.5Hz imaging frequency was low enough that the arrival of the CSD within the local region ROI and microglial ROI was simultaneous or within 1 frame of each other. However, this issue can become more significant if future imaging studies used significantly higher imaging frequencies. A potential expansion of the LRCT method would be to include a method of correcting for such misalignment through the use of covariance or similarity metrics to shift the local region and microglia traces such that the onset of the CSD occurs simultaneously.

CHAPTER 4

SEGMENTING THE WAVEFRONT BOUNDARIES OF CORTICAL SPREADING DEPRESSIONS

In this chapter, a method for segmenting the wavefront boundary of a cortical spreading depression is presented. This method uses a region-based local similarity metric in its energy function, but optimizes it over a distance map representation of the image as opposed to the traditional level set-based implementation. The results of this method are compared to results of other state-of-the-art and benchmark methods to demonstrate performance.

4.1 Local Similarity Metric Segmentation

In order to compensate for the high level of noise, intensity inhomogeneity, and wavefront occlusion present in confocal images of CSDs, we propose an modified version of level set segmentation which recontextualizes it from an malleable active contour to a threshold-based approach, which we call the Local Similarity Metric (LSM) method. The primary motivation of this method is to conserve the shape of the segmentation boundary between iterations,

preventing the final segmentation from being overly sensitive to discontinuities in the CSD wavefront that occur due to noise and occlusion. Furthermore, the LSM method seeks not to segment an object in an image from the background in the traditional sense, but rather to separate the image functionally into two regions: one where the neurons have depolarized in response to the CSD and one where they have yet to depolarize.

4.1.1 The Local Similarity Factor

The inspiration behind the LSM method is the local similarity factor (LSF). Introduced by Nui *et al.* [31], the LSF provides a distance-weighted, region-based measurement of the similarity between the intensities of pixels within a region and the region's mean intensity. For a given pixel, x, within an image, I, the LSF is defined as:

$$LSF(x, lc) = \int_{y \in N_x \neq x} \frac{|I(y) - lc|^2}{d(x,y)} dy \tag{4.1}$$

where N_x is a square-shaped window defining the local region, $d(x,y)$ is the Euclidean distance between pixels x and y, and lc is the local mean intensity. The LSF metric has two major advantages that are valuable for the problem addressed in this project. First, the method does not require preprocessing, in the form of noise reduction or contrast enhancement, for the metric to be effective. Second, the LSF-based model is robust to high levels of noise as well as intensity inhomogeneity, making LSF appealing for the CSD images this chapter focuses on [31].

Two different LSF values are computed per pixel for each iteration of the algorithm. LSF_1 compares pixels that are inside the current segmentation boundary, while LSF_2 compares pixels that are outside said boundary. As a result, two local mean intensities, lc_1 and lc_2, are calculated when evaluated over a level set function, $\phi(\cdot)$:

$$lc_1(x) = \frac{\int_\Omega M(x,y) I(y) H_\varepsilon(\phi(y)) dy}{\int_\Omega M(x,y) H_\varepsilon(\phi(y)) dy} \tag{4.2}$$

and

$$lc_2(x) = \frac{\int_\Omega M(x,y)I(y)(1-H_\varepsilon(\phi(y)))dy}{\int_\Omega M(x,y)(1-H_\varepsilon(\phi(y)))dy}. \tag{4.3}$$

$M(x,y)$ is a mask of the local region defined as

$$M(x,y)\begin{cases}1 & d(x,y)<r\\ 0 & else\end{cases} \tag{4.4}$$

and $H_\varepsilon(\cdot)$ is the regularized Heaviside function.

By combining equations (4.1-4.4), Nui *et al.* [31] produce the following energy functional, called the Region-based model via Local Similarity Factor (RLSF):

$$\begin{aligned} E^{RLSF}(x,\phi(x)) =& \lambda_1\int_\Omega LSF_1(x,lc_1(x))H_\epsilon(\phi(x))dx+\\ &+\lambda_2\int_\Omega LSF_2(x,lc_2(x))(1-H_\epsilon(\phi(x)))dx\\ &+\mu\int\delta_\epsilon(\phi(x))|\bigtriangledown\phi(x)|dx \end{aligned} \tag{4.5}$$

where $\delta_\epsilon(\cdot)$ is the regularized Dirac delta function and λ_1, λ_2, and μ are weighting terms. The last integral of the energy functional serves as a smoothing parameter, with larger values of μ resulting in a smoother contour.

4.1.2 Distance Map-Based Image Representation

In the LSM model, the boundary of a segmentation contour is defined according to a distance map representation of the image rather than a level set function. This normalized distance map, $D_I(x)$, is defined as:

$$D_I(x) = (2H_\epsilon(\phi_0(x))-1)\frac{d_0(x)g_0(x)}{max_{y\in\Omega}\{d_0(y)g_0(y)\}} \tag{4.6}$$

where d_0 and g_0 are normalized Euclidean and geodesic distance maps of the image, respectively, and $\phi_0(\cdot)$ is the user-defined initial contour. By incorporating the geodesic map, regions with significant shifts in pixel intensity

create regions where more distance traveled per iteration is necessary for significant alteration in the contour, improving convergence on well-defined wavefronts. The initial contour's boundary pixels, excluding those on the edges of the image, serve as the "zero-points" of both distance maps, meaning that the value of a pixel x is the shortest distance from it to one of the boundary pixels (Figure 4.1). In order to encourage a smooth curve shape over various threshold values, a median filter is applied to the map.

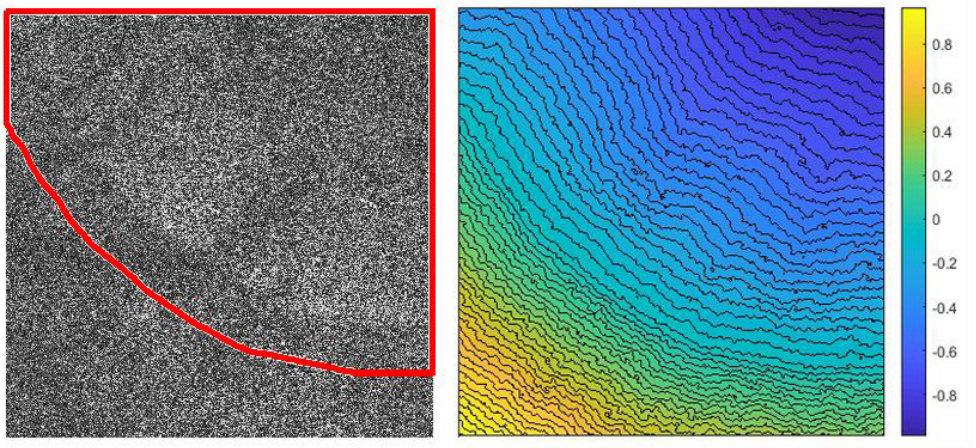

Figure 4.1: Example of a distance map (*right*) generated from an initial contour (*left*). Distances between pixels increase at the wavefront boundary.

4.1.3 Distance Map-Based Image Segmentation Through a Pseudo-Level Set Approach

The use of a distance map bears functional similarity to the level set approach used by many other segmentation algorithms. Like the level set, it is a higher-dimensional representation of the image which can be thresholded in order to form a desired contour. The critical difference compared to traditional level sets is its static nature. New contour boundaries can be generated by choosing different distances to threshold instead of iteratively altering the representation. This means that each new contour shares a similar general shape

to the previous contours, but is shifted shifted the image. This is advantageous for our purpose, as this rigidity in overall shape prevents the contour from deforming significantly and sinking into gaps in the CSD wavefront caused to inhomogeneity and noise. At the same time, its similarity to a level set function means that it can be easily implemented for segmentation in a level set-like manner.

Using the distance map generated by (4.6), we can define a pseudo-level set of the image, with respect to a given threshold T, as such:

$$\phi(x,T) = \begin{cases} 1 & D_I(x) \leq T \\ -1 & else. \end{cases} \tag{4.7}$$

Using this pseudo-level set, we define the LSM energy functional as follows:

$$\begin{aligned} &E^{LSM}(T) = \\ &\lambda_1 \int_\Omega LSF_1(x, lc_1(x)) H_\epsilon(\phi(x,T)) dx \\ &+ \lambda_2 \int_\Omega LSF_2(x, lc_2(x))(1 - H_\epsilon(\phi(x,T))) dx. \end{aligned} \tag{4.8}$$

Note that the smoothing term has been dropped from the original RLSF model (4.5), as the contour shape is strictly defined by D_I and the choice of T. A smooth contour is enforced through the use of Euclidean distance in generating D_I and the median filter applied to it. Furthermore, both lc_1 and lc_2, in (4.2-4.3), also use $\phi(x,T)$ instead of $\phi(x)$. For the sake of brevity, we will not explicitly redefine them here.

4.1.4 Threshold optimization through gradient descent

Once the initial contour has been defined and the appropriate distance map has been generated, the optimal threshold value for the image is calculated through the use of a gradient descent algorithm with a fast marching method-like implementation.

The partial differential equation used for the gradient descent algorithm is as follows:

$$\frac{\partial T}{\partial t} = \lambda_1 \int_{N_T} LSF_1(x, lc_1)dx - \lambda_2 \int_{N_T} LSF_2(x, lc_2)dx, \tag{4.9}$$

where N_T is a subset of the image containing pixels that are within a specified distance from the current threshold boundary. However, the curved geometry of the CSD wavefront often leads to an imbalance within N_T between the number of pixels outside versus inside the current threshold, which biases one side over the other. We equalize this imbalance by removing pixels on the overrepresented side from N_T.

In order to minimize (4.8), the following gradient descent formulation is utilized:

$$T_{n+1} = T_n + \Delta t \Delta T_n \tag{4.10}$$

where ΔT_n is a numerical approximation of (4.9). Δt is the step-size, defined as:

$$\Delta t = \frac{1}{N max_{x \in N_T}(LSF_1(x, lc_1) - LSF_2(x, lc_2))} \tag{4.11}$$

where N is the number of pixels within N_T.

4.2 Performance Evaluation

4.2.1 Dataset and parameter selection

In order to evaluate the performance of the LSM method, a dataset of twenty 512x512 pixel images of CSDs was compiled from the green channels of the calcium imaging sequences discussed in Chapter 3. Images from these sequences were selected such that the dataset contained a variety of possible noise and contrast levels, as well as various shapes that the CSD wavefront can assume. While it would have been beneficial to have had a larger dataset

for this analysis, the novelty of this imaging technique and the overall cost of such experiments limits the quantity and quality of sequences at our disposal.

As stated before, the algorithm requires several parameters to be specified by the user prior to segmentation. Given the resolution of our sequences, for the local window, N_x, a size of 17x17 pixels was selected, while the regional mask, M, had a radius of 13 pixels. For the region used to calculate the gradient descent, N_T, pixels within 7 pixels of the current boundary were considered. Finally, the weighting terms were set as $\lambda_1 = \lambda_2 = 1$. The geodesic distance map used in creating D_I was generated using the MATLAB (MathWorks, CA) command `imsegfmm`.

4.2.2 Comparison Methods and Performance Metrics

To evaluate the performance of the LSM method, the results were compared with that of Chan-Vese [2] and the Lagrange Level Set (L2S) method [3]. Chan-Vese is often considered a benchmark segmentation method for biomedical images, and is often included in performance evaluations. L2S is a local-region based method which is robust against intensity inhomogeneity [3]. The implementation of the L2S method used in this evaluation utilizes a fast-marching method approach which prevents contour edges that lie on the edges of an image from evolving. Chan-Vese segementation was performed with MATLAB's built in implementation, `activecontour`. Both L2S and Chan-Vese were executed for 1000 iterations, while LSM ran for only 50 iterations.

Performance was measured using two different metrics. The first was the DICE index, which measures the overlap between the segmentation result and the ground truth [29]. This is calculated as $DICE(R_1,R_2) = \frac{2Area(R_1 \cap R_2)}{Area(R_1)+Area(R_2)}$ where R_1 is the ground truth and R_2 is the segmentation. A DICE index closer to 1 indicates superior performance. However, due to the large area of the image being segmented, a poor segmentation can still result in a large DICE index. Therefore, we used the root mean square error (RMSE) as a second performance metric. Here, the error being measured is the Euclidean distance between a given point on the segmentation boundary and the nearest point

on the ground truth boundary. For the initialization, an initial contour was hand-drawn such that the only edge of the contour which did not lie on the image boundary was a rough approximation of the CSD wavefront, displaced approximately 40 pixels away from the wavefront boundary in the image. These initial segments had a mean DICE index of .9213 and a mean RMSE of 23.00 pixels.

4.2.3 Results & Discussion

Over the entirety of the dataset, the LSM method demonstrated superior performance compared to the other methods examined (Fig. 4.2 & 4.3). The LSM method yielded a mean DICE index of .986, compared to that of .931 and .814 for L2S and Chan-Vese, respectively. Likewise, LSM had a mean RMSE of 4.52 pixels, compared to 22.57 pixels and 30.19 pixels for L2S and Chan-Vese, respectively (Table 4.1).

The segmentation errors of L2S were largely characterized by the contour's inability to evolve towards the wavefront. It was often observed that only a portion of the active contour would shift towards the boundary of the wavefront, while the rest of the contour would remain static or change negligibly around the area it was initialized. In some cases, the contour would not evolve at all. This behavior was likely the result of the high SNR of the images, creating difficulties in calculating local information that would direct the level set towards the wavefront. By contrast, intensity inhomogeneity was the primary cause of failure for Chan-Vese. The active contour would converge around the

Table 4.1: Results of method comparison. Statistical significance between methods was calculated using a student t-test with respect to the LSM results.

	DICE			RMSE		
	Mean	StDev	p	Mean	StDev	p
LSM	0.986	0.013	-	4.53	3.66	-
L2S [3]	0.931	0.030	$7.08\ 10^{-9}$	22.57	3.93	$1.12\ 10^{-17}$
Chan-Vese [2]	0.814	0.203	$5.32\ 10^{-4}$	30.19	8.51	$6.52\ 10^{-15}$

brightest portions of the depolarized region, often excluding regions where noise and occlusion obscured the increased fluorescence. Since Chan-Vese has greater emphasis on the global relationship between object vs background pixel intensities [2], areas within the depolarized region with reduced fluorescence due to occlusion were often interpreted as part of the polarized region. This difficulty was often further extended areas regions significantly behind the wavefront that had reduced fluorescence, with the contour evolving away from the edges of the image towards the boundaries of such regions.

In contrast to L2S and Chan-Vese, the LSM method demonstrated a con-

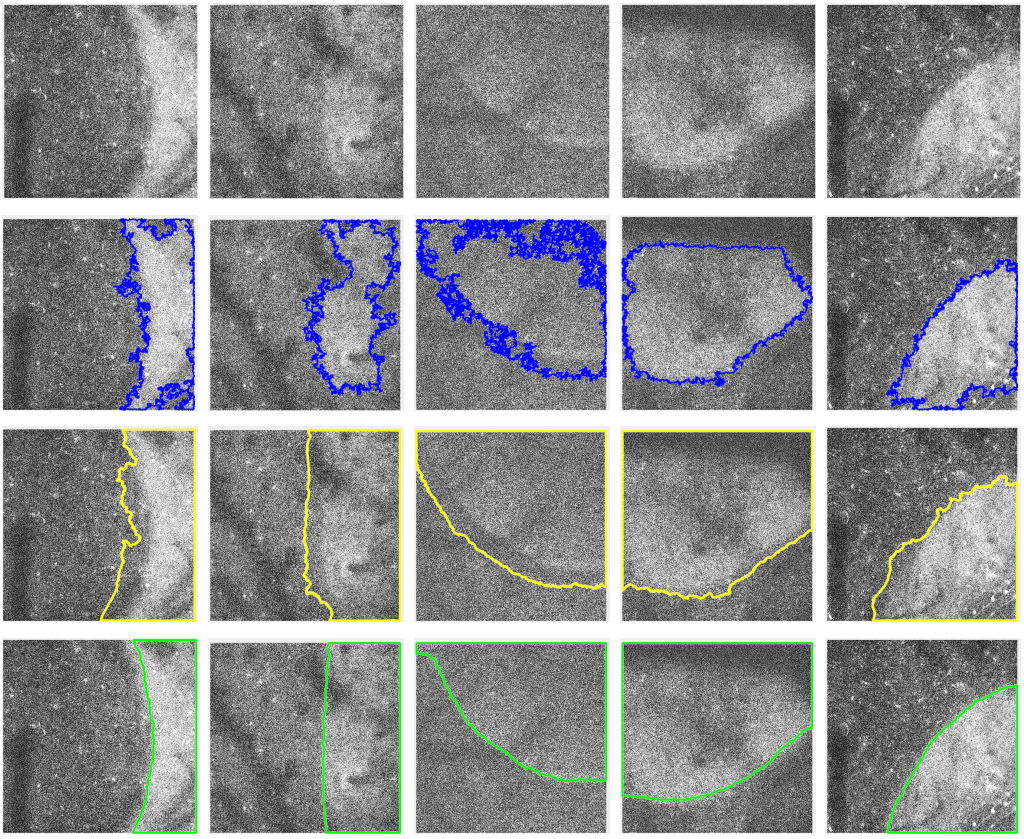

Figure 4.2: Segmentation results of CSD images. *(First row)* Raw calcium images of CSD. *(Second row)* Initialization. *(Third row)* Chan-Vese [2]. *(Fourth row)* L2S [3]. *(Fifth row)* LSM. Images have undergone post-segmentation contrast enhancement to improve visibility of CSD.

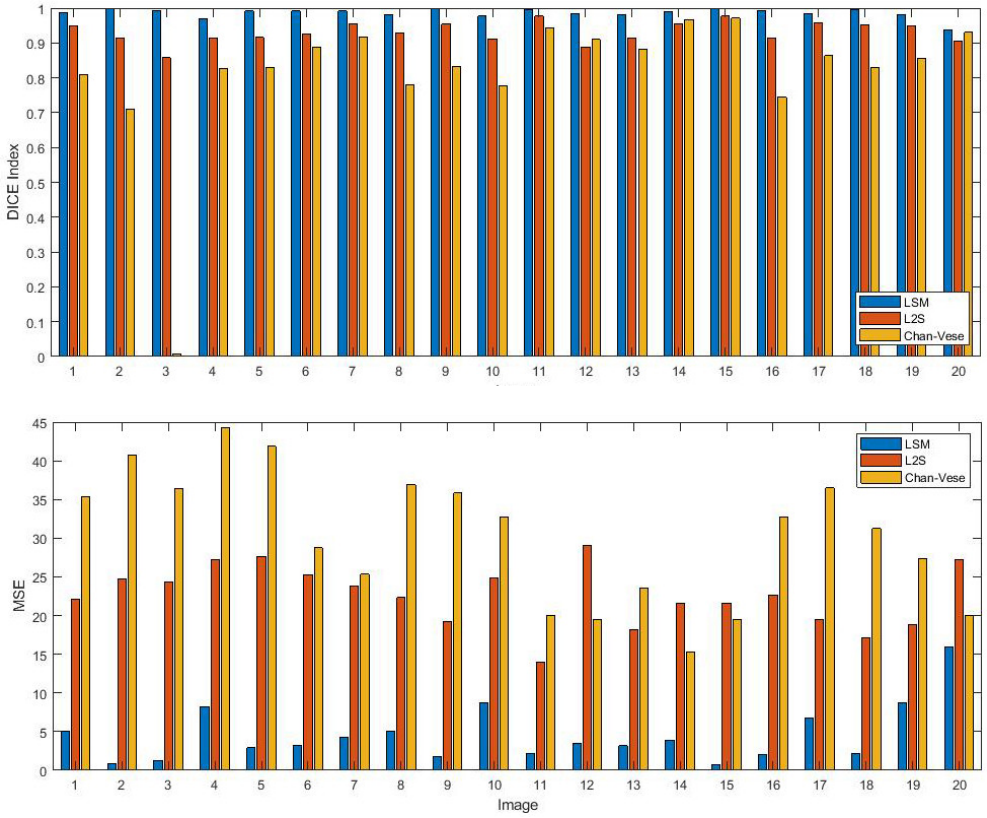

Figure 4.3: Segmentation results of CSD on individual images. (*top*) DICE Index. (*bottom*) MSE.

sistent ability to converge on the wavefront boundary accurately. This is likely due to a combination of using a local region-based metric to drive contour evolution and the rigid nature of these contours. As a result, it is able to evolve towards the boundary of the CSD without being susceptible to intensity inhomogeneity at the boundary. One downside that was noticed, particularly in images with significant inhomogeneity at the boundary, was a tendency for a slightly unstable convergence. Instead of remaining largely static once it reached the wavefront, the contour would, in some cases, begin to oscillate between underestimating and overestimating the boundary by small distances. This behavior is likely the result of the rigid nature of the contour. Calculating the LSF over the entirety of a contour boundary as one metric results in a

degree of sensitivity to inhomogeneity, whereby inhomogeneous regions exert a pressure for further evolution which drive the contour over the boundary, which is then compensated for in the next iteration. In traditional level set methods, this issue is resolved by the contour's malleable nature. For the LSM method, this issue could be resolved in future iterations by having a scaling step size that decreases over the course of optimization or with increasing convergence, thereby reducing the degree to which the contour can change as it converges to the boundary.

CHAPTER 5

CONCLUSION

5.1 Conclusions from chap 3

In this chapter, we presented a workflow that can assist researchers in analyzing microglial activation in response to CSDs. The efficacy of this method has been validated through use on a real-world experiment, bearing the results which were predicted in the literature. By adopting this general methodology, we hope that future researchers will have an easier, standardized method of conducting research on this topic and improve our understanding and treatments of stroke and traumatic brain injury. Despite the successes of the methods, there are still some challenges which can be improved upon in future work. The signal denoising process presented in the analysis workflow is sensitive to the timing between when the signal of the CSD appears in the local region and with the region of interest of a microglia. Future iterations may benefit from additional methods which correct for this though the use of similarity or covariance metrics to correct for this misalignment.

5.2 Conclusion from chap 4

In this chapter, a novel approach to segmenting wavefront boundaries in two-photon calcium images of CSDs is presented. Qualitative analysis of the performance for LSM indicates improvements in comparison to the state-of-the-art and benchmark. In addition to accurate segmentation results, the LSM method has a fast rate of convergence, requiring less than 50 iterations. The most significant downside of this method is its dependence on the user's *a priori* knowledge of the wavefront's shape, which limits throughput on larger datasets. Inclusion of the LSM into models which can incorporate *a priori* shape information in an adaptable manner is an appealing solution for future work. Additional issues with convergence stability can be addressed through the use of a decreasing step size during threshold optimization.

BIBLIOGRAPHY

[1] Petr Tvrdik and M Kalani,
"In vivo imaging of microglial calcium signaling in brain inflammation and injury,"
International journal of molecular sciences, vol. 18, no. 11, pp. 2366, 2017.

[2] Tony F Chan, B Yezrielev Sandberg, and Luminita A Vese,
"Active contours without edges for vector-valued images,"
Journal of Visual Communication and Image Representation, vol. 11, no. 2, pp. 130–141, 2000.

[3] Suvadip Mukherjee and Scott T Acton,
"Region based segmentation in presence of intensity inhomogeneity using legendre polynomials,"
IEEE Signal Processing Letters, vol. 22, no. 3, pp. 298–302, 2015.

[4] Jens P Dreier, Martin Fabricius, Cenk Ayata, Oliver W Sakowitz, C William Shuttleworth, Christian Dohmen, Rudolf Graf, Peter Vajkoczy, Raimund Helbok, Michiyasu Suzuki, et al.,
"Recording, analysis, and interpretation of spreading depolarizations in neurointensive care: review and recommendations of the cosbid research group,"
Journal of Cerebral Blood Flow & Metabolism, vol. 37, no. 5, pp. 1595–1625, 2017.

[5] Martin Fabricius, Susanne Fuhr, Robin Bhatia, Martyn Boutelle, Parastoo Hashemi, Anthony J Strong, and Martin Lauritzen,

"Cortical spreading depression and peri-infarct depolarization in acutely injured human cerebral cortex,"
Brain, vol. 129, no. 3, pp. 778–790, 2005.

[6] Atsushi Mizuma, Jong Youl Kim, Rachid Kacimi, Ken Stauderman, Michael Dunn, Sudarshan Hebbar, and Midori A Yenari,
"Microglial calcium release-activated calcium channel inhibition improves outcome from experimental traumatic brain injury and microglia-induced neuronal death,"
Journal of Neurotrauma, 2018.

[7] Gergely Szalay, Bernadett Martinecz, Nikolett Lénárt, Zsuzsanna Környei, Barbara Orsolits, Linda Judák, Eszter Császár, Rebeka Fekete, Brian L West, Gergely Katona, et al.,
"Microglia protect against brain injury and their selective elimination dysregulates neuronal network activity after stroke,"
Nature communications, vol. 7, pp. 11499, 2016.

[8] Mamoru Shibata and Norihiro Suzuki,
"Exploring the role of microglia in cortical spreading depression in neurological disease,"
Journal of Cerebral Blood Flow & Metabolism, vol. 37, no. 4, pp. 1182–1191, 2017.

[9] Christoph Stosiek, Olga Garaschuk, Knut Holthoff, and Arthur Konnerth,
"In vivo two-photon calcium imaging of neuronal networks,"
Proceedings of the National Academy of Sciences, vol. 100, no. 12, pp. 7319–7324, 2003.

[10] Kae M Pusic, Aya D Pusic, Jordan Kemme, and Richard P Kraig,
"Spreading depression requires microglia and is decreased by their m2a polarization from environmental enrichment,"
Glia, vol. 62, no. 7, pp. 1176–1194, 2014.

[11] Sebastian Jander, Michael Schroeter, Oliver Peters, Otto W Witte, and Guido Stoll,
"Cortical spreading depression induces proinflammatory cytokine gene expression in the rat brain,"
Journal of Cerebral Blood Flow & Metabolism, vol. 21, no. 3, pp. 218–225, 2001.

[12] Claudia Eder,
"Ion channels in microglia (brain macrophages),"
American Journal of Physiology-Cell Physiology, vol. 275, no. 2, pp. C327–C342, 1998.

[13] Amir Pozner, Ben Xu, Sierra Palumbos, J. Michael Gee, Petr Tvrdik, and Mario R. Capecchi,
"Intracellular calcium dynamics in cortical microglia responding to focal laser injury in the pc::g5-tdt reporter mouse,"
Frontiers in Molecular Neuroscience, vol. 8, pp. 12, 2015.

[14] Karl J Friston,
"Imaging neuroscience: Principles or maps?,"
Proceedings of the National Academy of Sciences, vol. 95, no. 3, pp. 796–802, 1998.

[15] Karel Svoboda and Ryohei Yasuda,
"Principles of two-photon excitation microscopy and its applications to neuroscience,"
Neuron, vol. 50, no. 6, pp. 823–839, 2006.

[16] Martin Oheim, Emmanuel Beaurepaire, Emmanuelle Chaigneau, Jerome Mertz, and Serge Charpak,
"Two-photon microscopy in brain tissue: parameters influencing the imaging depth,"
Journal of neuroscience methods, vol. 111, no. 1, pp. 29–37, 2001.

[17] Nilanjan Ray and Scott T Acton,
"Active contours for cell tracking,"
in *Image Analysis and Interpretation, 2002. Proceedings. Fifth IEEE Southwest Symposium on*. IEEE, 2002, pp. 274–278.

[18] A-R Mansouri, Dipti Prasad Mukherjee, and Scott T Acton,
"Constraining active contour evolution via lie groups of transformation,"
IEEE Transactions on Image Processing, vol. 13, no. 6, pp. 853–863, 2004.

[19] Scott T Acton and Nilanjan Ray,
"Biomedical image analysis: Segmentation,"
Synthesis Lectures on Image, Video, and Multimedia Processing, vol. 4, no. 1, pp. 1–108, 2009.

[20] Anthony S Wright and Scott T Acton,
"Watershed pyramids for edge detection,"
in *Image Processing, 1997. Proceedings., International Conference on*. IEEE, 1997, vol. 2, pp. 578–581.

[21] J Michael Gee, Nathan A Smith, Fernando R Fernandez, Michael N Economo, Daniela Brunert, Markus Rothermel, S Craig Morris, Amy Talbot, Sierra Palumbos, Jennifer M Ichida, et al.,
"Imaging activity in neurons and glia with a polr2a-based and cre-dependent gcamp5g-ires-tdtomato reporter mouse,"
Neuron, vol. 83, no. 5, pp. 1058–1072, 2014.

[22] Herbert Bay, Tinne Tuytelaars, and Luc Van Gool,
"Surf: Speeded up robust features,"
in *European conference on computer vision*. Springer, 2006, pp. 404–417.

[23] Olivier D Faugeras,
"What can be seen in three dimensions with an uncalibrated stereo rig?,"
in *European conference on computer vision*. Springer, 1992, pp. 563–578.

[24] Richard I Hartley,

"Estimation of relative camera positions for uncalibrated cameras,"
in *European conference on computer vision*. Springer, 1992, pp. 579–587.

[25] Philip HS Torr and Andrew Zisserman,
"Mlesac: A new robust estimator with application to estimating image geometry,"
Computer vision and image understanding, vol. 78, no. 1, pp. 138–156, 2000.

[26] Michael Kass, Andrew Witkin, and Demetri Terzopoulos,
"Snakes: Active contour models,"
International journal of computer vision, vol. 1, no. 4, pp. 321–331, 1988.

[27] Chenyang Xu, Jerry L Prince, et al.,
"Snakes, shapes, and gradient vector flow,"
IEEE Transactions on image processing, vol. 7, no. 3, pp. 359–369, 1998.

[28] Bing Li and Scott T Acton,
"Active contour external force using vector field convolution for image segmentation,"
IEEE transactions on image processing, vol. 16, no. 8, pp. 2096–2106, 2007.

[29] Olivier Bernard, Denis Friboulet, Philippe Thévenaz, and Michael Unser,
"Variational b-spline level-set: a linear filtering approach for fast deformable model evolution,"
IEEE Transactions on Image Processing, vol. 18, no. 6, pp. 1179–1191, 2009.

[30] James Albert Sethian,
Level set methods and fast marching methods: evolving interfaces in computational geometry, fluid mechanics, computer vision, and materials science, vol. 3,
Cambridge university press, 1999.

[31] Sijie Niu, Qiang Chen, Luis De Sisternes, Zexuan Ji, Zeming Zhou, and Daniel L Rubin,
"Robust noise region-based active contour model via local similarity factor for image segmentation,"
Pattern Recognition, vol. 61, pp. 104–119, 2017.

[32] Suvadip Mukherjee, Barry Condron, and Scott T Acton,
"Tubularity flow fieldâĂŤa technique for automatic neuron segmentation,"
IEEE Transactions on Image Processing, vol. 24, no. 1, pp. 374–389, 2014.

[33] Nikos Paragios and Rachid Deriche,
"Geodesic active regions and level set methods for supervised texture segmentation,"
International Journal of Computer Vision, vol. 46, no. 3, pp. 223–247, 2002.

[34] Chunming Li, Rui Huang, Zhaohua Ding, J Chris Gatenby, Dimitris N Metaxas, and John C Gore,
"A level set method for image segmentation in the presence of intensity inhomogeneities with application to mri,"
IEEE transactions on image processing, vol. 20, no. 7, pp. 2007–2016, 2011.

[35] Tiffany Ly, Jeremy Thompson, Tajie Harris, and Scott T Acton,
"The coupled tuff-bff algorithm for automatic 3d segmentation of microglia,"
in *2018 25th IEEE International Conference on Image Processing (ICIP)*. IEEE, 2018, pp. 121–125.

[36] Nobuyuki Otsu,
"A threshold selection method from gray-level histograms,"
IEEE transactions on systems, man, and cybernetics, vol. 9, no. 1, pp. 62–66, 1979.

[37] Jens Eilers, George J Augustine, and Arthur Konnerth,
"Subthreshold synaptic ca2+ signalling in fine dendrites and spines of cerebellar purkinje neurons,"
Nature, vol. 373, no. 6510, pp. 155, 1995.

[38] Félix Viana, Elvira De La Peña, Brian Pecson, Robert F Schmidt, and Carlos Belmonte,
"Swelling-activated calcium signalling in cultured mouse primary sensory neurons,"
European Journal of Neuroscience, vol. 13, no. 4, pp. 722–734, 2001.

[39] Saveez Saffarian, Yu Li, Elliot L Elson, and Linda J Pike,
"Oligomerization of the egf receptor investigated by live cell fluorescence intensity distribution analysis,"
Biophysical journal, vol. 93, no. 3, pp. 1021–1031, 2007.

[40] Iain M Johnstone, Bernard W Silverman, et al.,
"Needles and straw in haystacks: Empirical bayes estimates of possibly sparse sequences,"
The Annals of Statistics, vol. 32, no. 4, pp. 1594–1649, 2004.

[41] Ward Cheney and David Kincaid,
"Linear algebra: Theory and applications,"
The Australian Mathematical Society, vol. 110, 2009.

[42] Vladimir IïÿăAïÿąkovlevich Katkovnik, Karen Egiazarian, and Jaakko Astola,
"Local approximation techniques in signal and image processing,"
SPIE Bellingham, 2006.

[43] Geoffrey M Davis, Stephane G Mallat, and Zhifeng Zhang,
"Adaptive time-frequency decompositions,"
Optical engineering, vol. 33, no. 7, pp. 2183–2192, 1994.